PHYSICAL REVIEW B **95**, 184421 (2017)

Magnetic and magnetocaloric properties of $HoCrO_3$ tuned by selective rare-earth doping

Shiqi Yin,[1] Mohindar S. Seehra,[2] Curtis J. Guild,[3] Steven L. Suib,[3,4] Narayan Poudel,[5] Bernd Lorenz,[5] and Menka Jain[1,4,*]
[1]*Department of Physics, University of Connecticut, Storrs, Connecticut 06269, USA*
[2]*Department of Physics and Astronomy, West Virginia University, Morgantown, West Virginia 26506, USA*
[3]*Department of Chemistry, University of Connecticut, Storrs, Connecticut 06269, USA*
[4]*Institute of Materials Science, University of Connecticut, Storrs, Connecticut 06269, USA*
[5]*Texas Center for Superconductivity and Department of Physics, University of Houston, Houston, Texas 77204, USA*
(Received 16 February 2017; published 18 May 2017)

Rare-earth chromites ($RCrO_3$) are an important subclass of functional materials with interesting magnetic, electrical, and catalytic properties that make them promising for various applications. Here, we report comparisons on the structural and magnetic properties of $HoCrO_3$ with those of $Ho_{0.67}Tm_{0.33}CrO_3$ and $Ho_{0.67}Gd_{0.33}CrO_3$ powder samples, which were doped by Tm^{3+} (or Gd^{3+}) ions at the A-site with ionic radius smaller (or larger) than that of Ho^{3+} ion. The structural properties of the samples were characterized by x-ray diffraction, Raman spectroscopy, and scanning electron microscopy carried out at ambient. The band gaps of the three samples were determined by analyzing their ultraviolet Vis spectra. Magnetic studies carried out from 5 K to 300 K show that the Néel temperature (T_N^{Cr}, where Cr^{3+} ions order) increases with an increase in the average A-site (R-site) ionic radius, tolerance factor, and Cr1-O1-Cr1 bond angle but decreases with an increase in the orthorhombic strain factor. In addition, the application of external hydrostatic pressure was found to enhance T_N^{Cr} of $HoCrO_3$, similar to the effect observed by doping $HoCrO_3$ with Gd^{3+} ions. These changes in T_N^{Cr} with A-site doping and hydrostatic pressure are related to changes in Cr^{3+}-Cr^{3+} exchange coupling resulting from changes in the Cr1-O1-Cr1 bond angle and Cr1-O1 bond lengths, respectively. Temperature dependent paramagnetic susceptibility data of the samples was fitted to the modified Curie-Weiss law that included the Dzyloshinskii-Moriya interaction. Isothermal magnetization data showed that the magnetic behavior of the samples changes from canted antiferromagnetic at low temperatures to paramagnetic at higher temperatures. The large magnetocaloric entropy change was observed in $HoCrO_3$, which was enhanced by Gd doping but lowered by Tm doping, showing its tunability by A-site doping. Correlation between magnetoelectric properties and magnetization is discussed.

DOI: 10.1103/PhysRevB.95.184421

I. INTRODUCTION

Materials with more than one ferroic order—ferroelectricity (FE), ferromagnetism (FM), and ferroelasticity—are known as multiferroics [1–4]. Among the multiferroics, rare-earth chromites ($RCrO_3$, R = Ho, Er, Yb, Lu, and Y) are a type of magnetoelectric multiferroics with coexistence of FE and magnetic orders [5–8]. These $RCrO_3$ exhibit canted antiferromagnetism below the Néel temperatures ($T_N = 113$–140 K, depending on the R ion), while their FE transition temperatures (T_C) and associated mechanisms are still debated [5,9,10]. For example, Sahu *et al.* invoked the Curie-Weiss (CW) law by plotting the reciprocal of dielectric constant in the high-temperature region versus temperature data, and the T_C values were determined to be in the 472–516 K range for $HoCrO_3$, $ErCrO_3$, $YbCrO_3$, and $LuCrO_3$, independent of frequency [5]. However, Ghosh *et al.* reported a much lower T_C of 240 K for both $HoCrO_3$ bulk and thin films [11]. Similarly, the T_C of $SmCrO_3$ was reported to be 220 K, somewhat higher than its $T_N = 193$ K [12]. For $YCr_{0.5}Fe_{0.5}O_3$ samples, Rajeswaran *et al.* reported T_C and T_N to be nearly equal at 260 K [10].

The semiconducting nature of the $RCrO_3$ compounds has also attracted attention for photocatalytic and other light-harvesting applications [13–16]. Gupta and Poddar measured the ultraviolet-visible (UV-Vis) absorption spectra and explored the photocatalytic activity of $DyCrO_3$ nanoplatelets [13]. Some doped $RCrO_3$ compounds have also been investigated for hydrocarbon oxidation [17]. Compared to conventional photocatalytic materials such as TiO_2, $RCrO_3$ has advantages of strong absorption bands in the visible frequency range [18]. Doped $LaCrO_3$ perovskites are utilized in solid-oxide fuel cells due to their excellent energy conversion efficiency and high fuel flexibility resulting from the high operation temperatures [19,20]. In general, $RCrO_3$ compounds are p-type semiconductors with electronic sensitivity to humidity and gases (H_2, NO, N_2O, etc.), which makes them useful for sensor applications [21,22]. In addition, large magnetocaloric effects (MCEs) observed at temperatures below 30 K render some $RCrO_3$ compounds useful for applications in low-temperature magnetic refrigeration [16,23–26].

Various interesting properties of the $RCrO_3$ compounds with orthorhombically distorted perovskite (ABO_3) structures stem from strong correlations among their structural, electric, and magnetic properties [27]. In general, the perovskite structure can accommodate host ions with a range of ionic radii, which makes chemical substitution/doping an effective way to tune their structural and magnetic properties. For example, Sharma *et al.* reported that Dy and Ho doping at the Tb site in $TbMnO_3$ increases Mn-O-Mn bond angles and induce weak FM at 60 K and 63 K, respectively [28]. With the isostructure as $TbMnO_3$, $RCrO_3$ compounds contain corner-shared CrO_6 octahedra with the Cr^{3+} ions

---

[*] Author to whom correspondence should be addressed: menka.jain@uconn.edu

in the center and R^{3+} ions occupying vacant sites between the CrO_6 octahedral sites. The mismatch between R-O and Cr-O bond lengths in the Goldschmidt tolerance factor ($t = (r_{R^{3+}} + r_{O^{2-}})/\sqrt{2}(r_{Cr^{3+}} + r_{O^{2-}}) < 1$) leads to considerable co-operative rotations of the CrO_6 octahedra, which decreases with increasing R^{3+} ionic radius. With rare-earth dopants on the A-site (i.e., R-site), Cr1-O1-Cr1 bond angles in $RCrO_3$ is expected to change, similar to those in orthorhombic $RMnO_3$ [28,29]. Therefore, it would be interesting to study the dependence of the structural and magnetic properties of $RCrO_3$ with chemical doping (chemical pressure) and/or applying external hydrostatic pressure. Recently, Fe doping at the Cr-site of $DyCrO_3$ and $HoCrO_3$ was found to enhance their respective T_N and affect their magnetocaloric properties at low temperatures [16,24]. McDannald and Jain also reported that Ho and Y doping on the A-site lowers the MCE of $DyCrO_3$ powder samples, while Er doping improves the MCE [25]. It should be noted that the application of external pressure in compounds with distorted perovskite structures is an alternate approach to modify structural distortions, as reported for $DyMnO_3$ [30] and $RCrO_3$ [31], along with the theoretical reports on structural distortions in $RFeO_3$ [32] and structural/magnetization behavior in $RCrO_3$ [33] recently. However, experimental investigations on the effect of pressure on magnetic properties of $RCrO_3$ are still lacking.

To our knowledge, the effects of chemical pressure (i.e., by doping at the A-site) of $HoCrO_3$ on its structural, optical, and magnetic properties and effect of hydrostatic pressure on its magnetic property have not been reported yet. Hence, our aim in the present paper is to experimentally explore the effect of A-site doping on the structural and magnetic properties of $HoCrO_3$ bulk samples with an emphasis on the changes of their MCE properties. To explore both ends of the induced chemical pressure, we chose to substitute the A-site in $HoCrO_3$ with two rare-earth ions, Tm^{3+} and Gd^{3+}, which have smaller and larger ionic radius than that of Ho^{3+}, respectively. The compositions that are studied here are $Ho_{0.67}Tm_{0.33}CrO_3$, $HoCrO_3$, and $Ho_{0.67}Gd_{0.33}CrO_3$. In addition, the effect of hydrostatic pressure on the magnetic properties of bulk $HoCrO_3$ sample is also reported. It was found that the A-site doping with a larger ion (than Ho^{3+}) had a similar effect as the application of external hydrostatic pressure on the magnetic properties of $HoCrO_3$.

II. EXPERIMENTAL PROCEDURES

To prepare $Ho_{0.67}Tm_{0.33}CrO_3$ (HTCO), $HoCrO_3$ (HCO), and $Ho_{0.67}Gd_{0.33}CrO_3$ (HGCO) powder samples, first $Ho(NO_3)_3$, $Tm(NO_3)_3$, $Gd(NO_3)_3$, and $Cr(NO_3)_3$ precursors (99.999% purity) were dissolved in water in stoichiometric ratios and then mixed in a beaker using magnetic stirrer on a hot plate. Then, after the addition of citric acid, the three solutions were dried, and the resultant powders were annealed at 900°C in oxygen environment for 2 hours each. The structure and phase purity of the samples were investigated by room-temperature x-ray diffraction (XRD) (Bruker D2) and Raman spectroscopy (Renishaw System 2000). Scanning electron microscopy (SEM) images were obtained using a JEOL JSM-6335F instrument. Energy-dispersive x-ray spectroscopy (EDS) was recorded to verify the chemical composition by an energy dispersive spectrometer attached to an FEI Teneo low vacuum scanning electron microscope. Optical absorbance was measured with a diffuse reflectance integrating sphere attached to a Shimadzu UV-2450 UV-Vis spectrometer. The UV-Vis measurements were performed by dispersing the sample in barium sulfate, which was also used as a reflective reference. The dc and ac magnetization measurements were performed by vibrating sample magnetometer and ac magnetic system attached to the Evercool Physical Property Measurement System (PPMS; Quantum Design), respectively. For the hydrostatic pressure measurements, first the powder samples were mixed with polyvinyl alcohol (PVA) solution as the binder and then dried. The resultant powder was then compressed into a pellet with a dye, followed by annealing at 1300 °C for 4 hours in air. A small piece of the pellet was cut and wound with insulated copper wire. After two layers of thinner wire (secondary coil) were wound on the top of it, two layers of thicker wire (primary coil) were wound. The sample and thermocouple was placed inside a Teflon tube where the contact wires were taken out from the copper cap. The Teflon tube with the sample was inserted into a Be-Cu cylinder supplied with two pistons on the top and bottom. The cylinder was inserted into the pressure cell, and pressure was applied with a hydraulic press [34]. The pressure cell was screwed to the probe and inserted into a wide mouth Dewar filled with liquid nitrogen. The temperature was controlled by lowering or raising the probe in the Dewar and measured using a chromel/alumel thermocouple. The rate of cooling and warming rate ranged from 1–3 K per minute. The sample pressure was estimated from the calibration curve of the pressure cell. The excitation current was driven in the primary coil, and the mutual inductance signal in the secondary coil was measured with a 19 Hz, LR 700 AC resistance bridge. When the magnetic properties of the sample changes, an anomaly in the mutual inductance of secondary coil is observed.

III. RESULTS AND DISCUSSION

A. Structural characteristics

Figure 1(a) shows the XRD patterns of the present samples. All the major peaks for each sample could be indexed based on an ortho-rhombically distorted perovskite structure with space group *Pbnm*. Thus, these samples were determined to be phase pure within the detection limit of laboratory XRD. Rietveld refinement was used to analyze the XRD data for each composition. A representative Rietveld refined pattern of the HTCO sample is shown in Fig. 1(b). The lattice parameters a, b, and c of the present samples obtained from the Rietveld refinement are listed in Table I; these agree well with the reported values for $HoCrO_3$, $TmCrO_3$, and $GdCrO_3$ [35]. It was found that [as shown in Fig. 1(c)] the lattice parameters of $HoCrO_3$ decrease with Tm doping and increase with Gd doping. This difference could be interpreted by the effect of dopant on the average A-site ionic radius $R_{\text{avg}} = \sqrt{0.33 * R^2_{\text{Tm/Gd}} + 0.67 * R^2_{\text{Ho}}}$ for HTCO and HGCO samples. Here R_{Tm}, R_{Ho}, and R_{Gd} are 1.052 Å, 1.072 Å, and 1.107 Å, respectively. As shown in Figs. 1(c) and 1(d), the lattice parameters a, b, c, and cell volume (V) increase with increase in R_{avg}, which matches

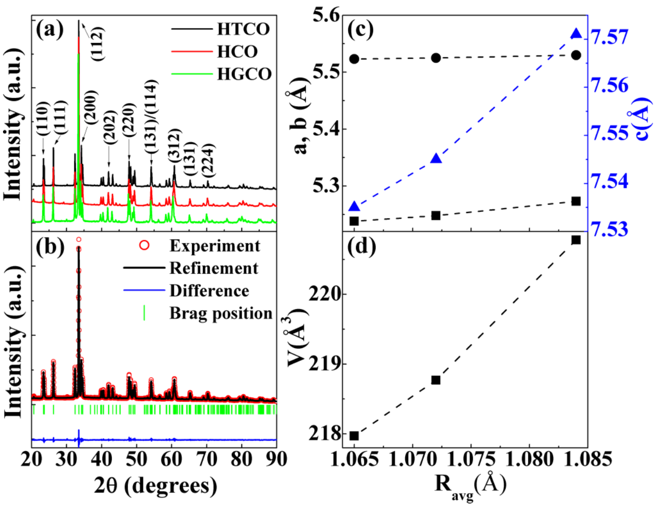

FIG. 1. (a) The x-ray diffraction data of $Ho_{0.67}Tm_{0.33}CrO_3$ (HTCO), $HoCrO_3$ (HCO), and $Ho_{0.67}Gd_{0.33}CrO_3$ (HGCO) samples. (b) Representative x-ray diffraction data and Rietveld refinement results of HTCO; A-site ionic radius (R_{avg}) dependence of the lattice parameters a (squares), b (circles), and c (triangles) is shown in (c) and that of the volume of the unit cell (V) in (d) with the lines connecting the data points as visual guides.

well with the experimental [35,36] and computational work [33]. From Rietveld refinement, the in-plane Cr1-O1-Cr1 bond angle, Cr1-O1 bond length, and atomic positions were also determined (see Table I). Note that the in-plane Cr1-O1-Cr1 bond angle increases with increasing R_{avg}, in agreement with the computational results [33].

Table I also summarizes the value of the aforementioned Goldschmidt tolerance factor (t) and the orthorhombic distortions (S) of the unit cells from the cubic structure characterized by $S = 2(b - a)/(b + a)$. With increasing R_{avg}, t increases, but S decreases. The crystallite size L of the powder samples were estimated using the Scherrer equation: $L = K\,\lambda/(\beta\cos\theta)$ [37,38]. Here β is the full width at half maximum (FWHM) of a diffraction peak in radians after subtracting the instrumental line broadening, θ is the Bragg angle, $K \approx 0.89$ is a dimensionless shape factor, and λ is the x-ray wavelength. Using the Fityk software [39], β was obtained by Pearson 7 peak fitting of the (hkl) peaks in the XRD data. The values of L of the present samples, calculated to be around 100 nm, are also listed in Table I.

The SEM images elucidating the surface morphology of HTCO, HCO, and HGCO samples are shown in Figs. 2(a)–2(c). No obvious impurity was found in these samples. A representative EDS spectrum of HTCO is shown in Fig. 2(d). The x-ray detector counts were quite high, yielding decent signal-to-noise ratios for the detection of O, Cr, Ho, and Tm.

In order to further examine the phase purity and structural characteristics of the samples, their Raman spectra measured at room temperature are shown in Fig. 3(a). The phonon Raman modes are labeled according to prior reports on RCrO$_3$ systems [40,41]. Among the 24 Raman active modes ($7A_g + 5B_{1g} + 7B_{2g} + 5B_{3g}$) according to group theory, 12 modes within 100–600 cm^{-1} range for the orthorhombic $Pbnm$

TABLE I. Lattice parameters, average A-site ionic radius (R_{avg}), Goldschmidt tolerance factor (t), orthorhombic strain (S), Cr1-O1-Cr1 bond angles, Cr1-O1 bond length, and atomic positions obtained from Rietveld refinement of the experimental XRD data, along with the average crystallite size (L) calculated by the Scherrer equation [$L = K\,\lambda/(\beta\cos\theta)$] for the present samples.

Sample		$Ho_{0.67}Tm_{0.33}CrO_3$	$HoCrO_3$	$Ho_{0.67}Gd_{0.33}CrO_3$
a(Å)		5.23794(3)	5.24825(5)	5.27317(7)
b(Å)		5.52291(3)	5.52519(5)	5.53024(9)
c(Å)		7.53471(4)	7.54501(7)	7.57100(9)
V(Å^3)		217.97(1)	218.78(1)	220.78(1)
R_{avg}(Å)		1.065	1.072	1.084
T		0.865	0.867	0.872
S		0.052964(1)	0.051421(1)	0.047591(1)
Cr1-O1-Cr1 (deg)		146.38	146.64	148.12
Cr1-O1 (Å)		1.968	1.975	1.968
Cr1-O2 (Å)		1.994	2.010	2.009
Cr1-O2 (Å)		1.986	1.966	1.974
Ho/R (4c)	x/a	−0.01812(21)	−0.01718(24)	−0.01684(27)
	y/b	0.06658(10)	0.06542(10)	0.06337(11)
	z/c	0.25000	0.25000	0.25000
Cr (4c)	x/a	0.50000	0.50000	0.50000
	y/b	0.00000	0.00000	0.00000
	z/c	0.00000	0.00000	0.00000
O1 (4c)	x/a	0.1018(98)	0.1040(95)	0.09591(113)
	y/b	0.4641(91)	0.4602(83)	0.4655(100)
	z/c	0.25000	0.25000	0.25000
O2 (4c)	x/a	−0.30735(77)	−0.30117(73)	−0.30272(88)
	y/b	0.30270(80)	0.30182(75)	0.30250(90)
	z/c	0.05388(52)	0.05501(50)	0.05237(59)
L (nm)		96(12)	104(13)	99(11)

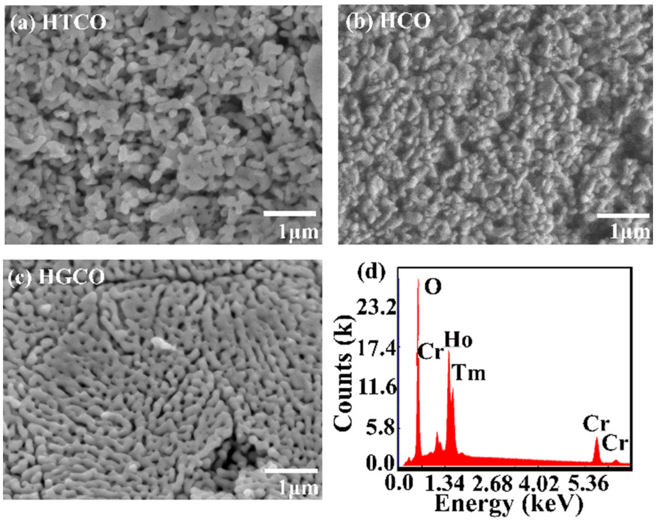

FIG. 2. Scanning electron microscopy images of (a) $Ho_{0.67}Tm_{0.33}CrO_3$ (HTCO), (b) $HoCrO_3$ (HCO), and (c) $Ho_{0.67}Gd_{0.33}CrO_3$ (HGCO) samples. (d) Energy-dispersive x-ray spectroscopy of the HTCO sample shows the presence of Ho, Tm, Cr, and O elements.

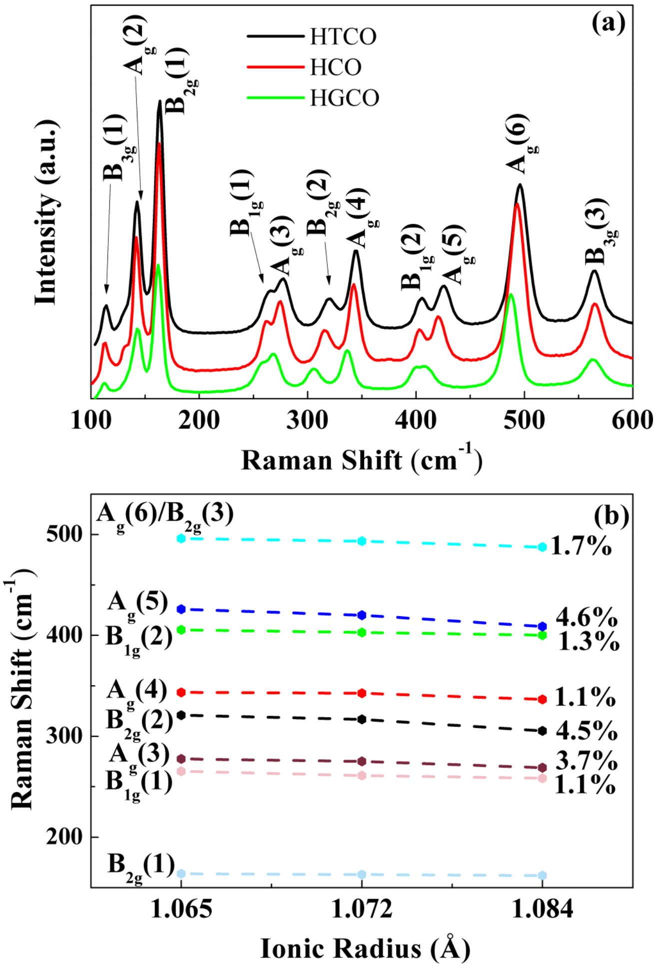

FIG. 3. (a) Raman spectra of $Ho_{0.67}Tm_{0.33}CrO_3$ (HTCO), $HoCrO_3$ (HCO), and $Ho_{0.67}Gd_{0.33}CrO_3$ (HGCO) samples. (b) Raman shift of phonon modes as a function of A-site ionic radius (R_{avg}, in angstrom) of HTCO, HCO, and HGCO. The dashed lines are visual guides connecting the data points with the number next to each line representing the percentage decrease of the line positions with increase in R_{avg}.

perovskite structure are present. The positions of the Raman modes of the three samples investigated here are compared in Table II and are plotted in Fig. 3(b). For the $A_g(2)$ and $B_{2g}(1)$ modes, the line positions are essentially unchanged within experimental uncertainties for the three samples. These modes with line positions below 200 cm^{-1} are due to A-O vibrational frequencies involving the heavier A atoms (Tm, Ho, Gd). Since the change in A-site mass in going from HTCO to HGCO is about 2% and the frequency varies inversely as the square root of mass, the frequency shift expected from this effect is about 1%, assuming no change in the coupling constant. The position of all the other Raman modes shifts to lower frequencies in going from the sample HTCO to HCO to HGCO, for which R_{avg} increases in the same order of the samples. The maximum percentage decrease of the line shifts for the three samples from HTCO to HGCO, listed in Fig. 3(b), is as high as 4.6% for the $A_g(5)$ mode. This decrease of the frequency shifts with increasing R_{avg} is in good agreement with the report of Weber *et al.* [40], in which extensive discussion on the assignment of the various Raman modes is also provided. The important result from this discussion is that the R_{avg}-dependent shift is correlated with the main structural distortion of in-plane O-Cr-O bond angles and hence octahedral tilting [40]. The broadening of some Raman modes evident in Fig. 3(a) for the HTCO and HGCO samples as compared to those in the HCO sample may be due to the inhomogeneity of the atoms on the A-site due to doping.

Bhadram *et al.* [41] have investigated the temperature dependence of the Raman modes in a number of $RCrO_3$ systems and reported that anomalies in the linewidth of Raman modes around T_N is observed only if R^{3+} is a magnetic ion such as Gd^{3+}, signaling the presence of spin-coupling via the R^{3+}-Cr^{3+} exchange coupling. Since this R^{3+}-Cr^{3+} exchange coupling is weaker than the Cr^{3+}-Cr^{3+} exchange coupling, its effect on the Raman modes at room temperature is likely not observable.

B. Optical absorption

The optical absorbance of the samples was measured in the wavelength range of 200–800 nm, and the results are presented in Figs. 4(a)–4(c). In $RCrO_3$, the energy states are composed of the R^{3+}-$4f$ level, the filled O^{2-}-$2p$ band, the partially filled Cr^{3+}-$3d$, and the empty Cr^{3+}-$4s$ band [13]. The peak at 455.5 nm results from the $^4A_2$ to $^4T_2$ transition, whereas the peak at around 610 nm is attributed to the $^4A_2$ to $^4T_1$ transition following the report of Gupta and Poddar [13]. Moreover, due to the high sensitivity of our system, peaks at around 300 nm, which were not reported by Gupta and Poddar, are interpreted by the $4f$-$5d$ and charge transfer transitions [13]. The overall shift between the peak positions may be explained by the difference of R_{avg}.

TABLE II. Positions and assignment of the Raman modes in $Ho_{0.67}Tm_{0.33}CrO_3$ (HTCO), $HoCrO_3$ (HCO), and $Ho_{0.67}Gd_{0.33}CrO_3$ (HGCO) powder samples.

Sample	$A_g(2)$	$B_{2g}(1)$	$B_{1g}(1)$	$A_g(3)$	$B_{2g}(2)$	$A_g(4)$	$B_{1g}(2)$	$A_g(5)$	$A_g(6)$	$B_{3g}(3)$
$Ho_{0.67}Tm_{0.33}CrO_3$	142.58(21)	163.76(32)	265.41(26)	277.06(40)	319.28(36)	343.50(42)	405.48(44)	426.05(34)	495.95(28)	565.31(47)
$HoCrO_3$	141.79(30)	162.96(27)	261.13(15)	275.07(38)	315.02(29)	342.70(44)	402.97(51)	420.11(39)	493.45(41)	564.51(47)
$Ho_{0.67}Gd_{0.33}CrO_3$	142.57(34)	161.99(28)	258.44(30)	267.12(27)	305.41(35)	336.59(37)	400.33(41)	407.20(38)	487.46(46)	561.94(45)

The optical absorption edge is related to the band energy, and the energy band gap (E_g) can be calculated by Tauc's equation [42,43],

$$\alpha h\nu = A(h\nu - E_g)^n. \qquad (1)$$

Here α is the optical absorption coefficient, $h\nu$ is the energy of the incident photon, A is a characteristic parameter, and $n = 1/2$ (2) for direct (indirect) transitions. Based on this equation, Figs. 4(d)–4(f) show the plots of $(\alpha h\nu)^2$ versus $h\nu$ for the three samples, and the linear absorption-edge curve was fitted with a straight line, the intersection of which with the $(\alpha h\nu)^2 = 0$ axis gives values of E_g as ~3.06, 3.14, and 2.75 eV, for HTCO, HCO, and HGCO bulk samples, respectively. Both Tm and Gd doping is found to lower the E_g of the HCO sample. Clearly, E_g of the HGCO sample is smaller than that of the HCO sample but slightly larger than that of the $GdCrO_3$ sample (2.7 eV) [44], i.e., in between the two end members, corroborating the doping/substitution effect. Additionally, E_g of the HCO sample is almost equal to the calculated value of 3.1 eV [16] but is slightly smaller than what Kotnana and Jammalamadaka experimentally reported (3.26 eV) [15]. These results, along with E_g values of the other $RCrO_3$ compounds from the literature, are summarized in Table III. Thus, it can be clearly seen that the band gap of HCO may be simply tuned by A-site doping by various rare-earth ions, signifying its potential application as a photocatalyst.

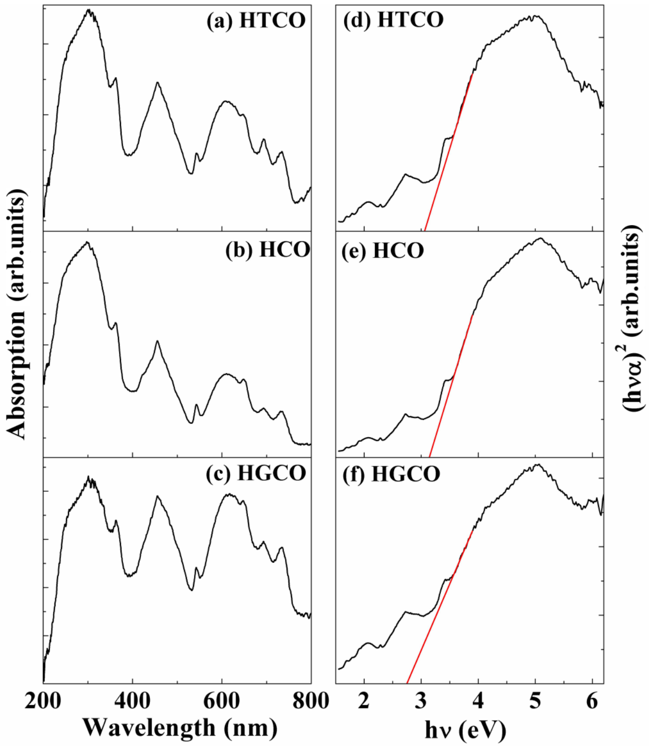

FIG. 4. Optical absorption spectra of (a) $Ho_{0.67}Tm_{0.33}CrO_3$ (HTCO), (b) $HoCrO_3$ (HCO), and (c) $Ho_{0.67}Gd_{0.33}CrO_3$ (HGCO) samples along with the respective (d)–(f) plots of $(\alpha h\nu)^2$ versus $h\nu$ for the samples following Eq. (1) with the extrapolated red line determining the direct energy gap.

C. Magnetic properties

Temperature dependence of the dc magnetic susceptibility ($\chi = M/H$, where M is the magnetization in emu/g and H is the applied magnetic field) for the three samples measured at a magnetic field $H = 50$ Oe (1 Oe $= 10^{-4}$ T) in field cooled (FC) modes is plotted in Fig. 5(a). At 5 K, the magnitudes of χ are 0.344, 0.593, and 0.363 emu g^{-1} (emu $g^{-1} = Am^2\,kg^{-1}$) for HTCO, HCO, and HGCO bulk samples, respectively. Their relative magnitudes can be explained by the differences in the magnetic moments (μ) of Ho^{3+} (10.4 μ_B), Tm^{3+} (7.57 μ_B), and Gd^{3+} (7.94 μ_B). As $\mu(Tm) < \mu(Gd) < \mu(Ho)$, HTCO and HCO samples show the smallest and largest value of χ, respectively. With increasing temperature, magnitudes of χ of the present samples decrease and then drop rapidly to very low values at a characteristic temperature ~150 K, followed by a very slow decrease thereafter. This characteristic temperature is the ordering temperature of the Cr^{3+} ions, namely the Néel temperature (T_N^{Cr}). To accurately determine T_N^{Cr}, the temperature variation of χT data was utilized because in antiferromagnets near T_N, the temperature variation of $d(\chi T)/dT$ is similar to that of heat capacity [48]. Figure 5(b) presents the temperature dependent $d(\chi T)/dT$ data, from the minimum of which T_N^{Cr} is determined to be 134 K, 139 K, and 148 K for HTCO, HCO, and HGCO bulk samples, respectively. These are consistent with the corresponding values reported for the end member compositions: 140 K, 125 K, and 167 K for $HoCrO_3$ [16], $TmCrO_3$ [35], and $GdCrO_3$ [26]. Importantly, these results show that T_N^{Cr} of HCO is lowered by doping at the A-site with Tm^{3+} (ionic radius smaller than that of Ho^{3+}) but increases by doping with Gd^{3+} with ionic radius larger than that of Ho^{3+}. Interpretation of this important result is presented later in this paper.

As mentioned above, the structural and magnetic properties of $RCrO_3$ are significantly dependent on R_{avg}, and T_N^{Cr} increases with an increasing R_{avg} [36]. To clearly demonstrate the dopant effect, the dependence of T_N^{Cr} on R_{avg}, the tolerance factor (t), orthorhombic strain (S), and the Cr1-O1-Cr1 bond angles are plotted in Fig. 6, in which the black triangles represent the data of our samples of HTCO, HCO, and HGCO and the red squares represent the data of $GdCrO_3$, $NdCrO_3$, and $LaCrO_3$ taken from the literature [36,40]. It is evident that T_N^{Cr} increases almost linearly with the increasing value of

TABLE III. A comparison of the energy band gap (E_g) of some rare-earth chromites (RCrO$_3$) obtained experimentally (Ex) or theoretically (Th).

Sample	$DyCrO_3$		$LaCrO_3$		$HoCrO_3$		$NdCrO_3$	$Ho_{0.67}Tm_{0.33}CrO_3$	$HoCrO_3$	$Ho_{0.67}Gd_{0.33}CrO_3$	$GdCrO_3$
E_g(eV)	2.8	2.7	3.4		3.26	3.1	1.78	3.06(7)	3.14(6)	2.75(6)	2.7
Method	Ex	Th	Ex	Th	Ex	Th	Ex	Ex	Ex	Ex	Ex
Reference	[13]	[16]	[45]	[46]	[15]	[16]	[47]	This paper			[44]

R_{avg}, t, and the Cr1-O1-Cr1 bond angle but decreases with the increase in the value of S. Thus, it can be inferred that the T_N^{Cr} of RCrO$_3$ compounds is related to distortions in the crystal structure and can be tuned by appropriate rare-earth doping.

Next, the effect of hydrostatic pressure on the Néel temperature of the HCO bulk sample was investigated by measuring the relative temperature dependence of mutual inductance under different hydrostatic pressures (0–16.5 kbar). When the magnetization of the sample changes, an anomaly in the mutual inductance of secondary coil is observed. As shown in Fig. 7(a), the sharp increase in the slope of the curve results from the magnetic ordering of Cr^{3+} ions, with T_N^{Cr} determined by the peak position. As shown in Fig. 7(b), T_N^{Cr} increases with increasing pressure, which agrees well with the results of RCrO$_3$ obtained theoretically [33]. Similarly, Poudel *et al.* reported that the Néel temperature of multiferroic GdMn$_2$O$_5$ single crystal increases with increasing hydrostatic pressure [49]. In addition, Alonso *et al.* observed that the external pressure induces structural changes in RMnO$_3$ samples, yielding larger Mn-O-Mn bond angles and tolerance factors [50]. Therefore, the application of external pressure in HoCrO$_3$ plays a similar role qualitatively as introducing a larger radius dopant, such as Gd in the present case.

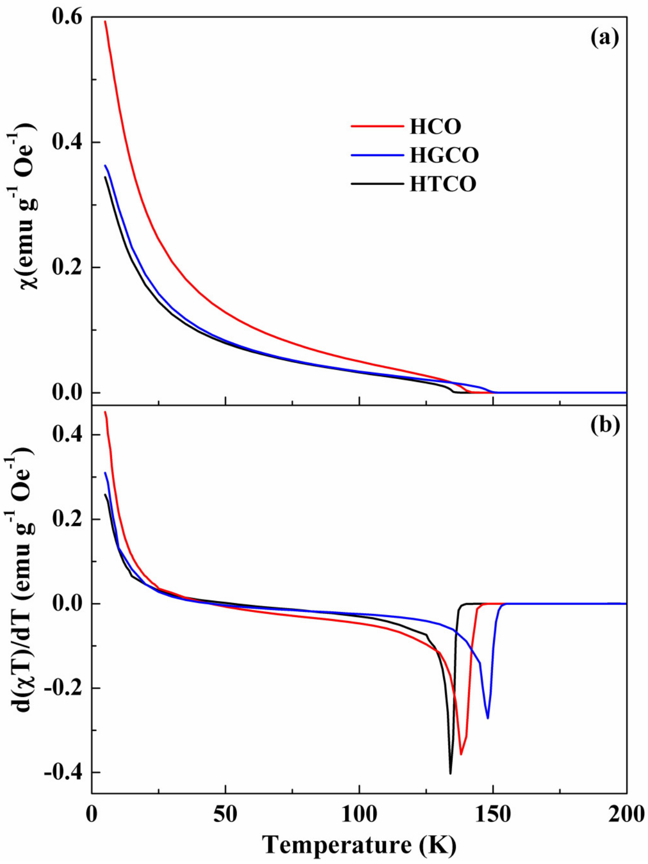

FIG. 5. (a) Temperature dependence of the magnetic susceptibility (χ) of Ho$_{0.67}$Tm$_{0.33}$CrO$_3$ (HTCO), HoCrO$_3$ (HCO), and Ho$_{0.67}$Gd$_{0.33}$CrO$_3$ (HGCO) measured in $H = 50$ Oe. (b) Plots of [$d(\chi T)/dT$] versus T from 5 to 200 K to determine T_N^{Cr}, the ordering temperature of Cr^{3+} moments.

A quantitative interpretation of the temperature dependence of the magnetic susceptibility above the Néel temperature T_N^{Cr} due to the ordering of Cr^{3+} ions is presented next by first fitting the data to the Curie-Weiss (CW) law: $\chi = C/(T - \theta)$ (C is the Curie constant, θ is the Weiss temperature). The temperature dependent $1/\chi$ data and the CW fittings are shown in Figs. 8(a)–8(c). With the fitted C value, the effective magnetic moment was then calculated using Eq. (2),

$$\mu_{\rm eff} = \sqrt{\frac{3k_B C}{N}}, \tag{2}$$

where k_B is the Boltzmann constant and $N = N_A$/molecular weight (MW) is the number of magnetic ions per gram of the sample [51]. Alternatively, the effective magnetic moment $\mu_{\rm eff}{}^a$ can be calculated using the free ionic moments of Ho^{3+},

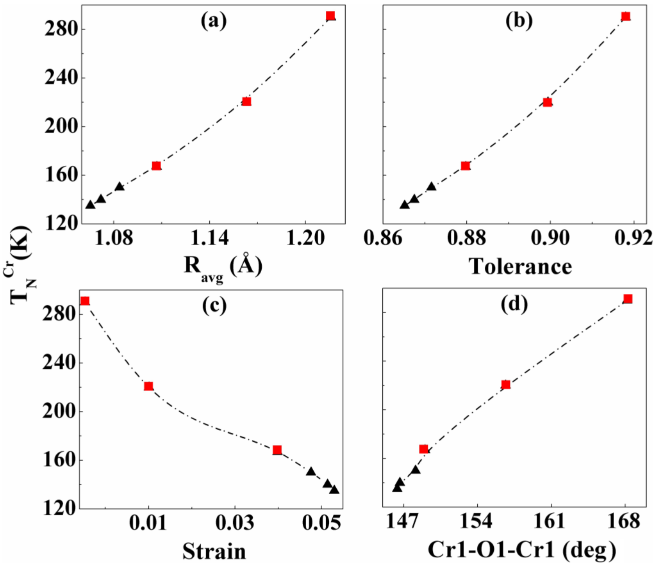

FIG. 6. The dependence of Néel temperature (T_N^{Cr}) on (a) average radii of A-site ions (R_{avg}), (b) tolerance factor (t), (c) orthorhombic strain (S), and (d) the in-plane Cr1-O1-Cr1 bond angle. The black triangles represent the data of the present Ho$_{0.67}$Tm$_{0.33}$CrO$_3$, HoCrO$_3$, and Ho$_{0.67}$Gd$_{0.33}$CrO$_3$ samples, and the red squares represent the data of GdCrO$_3$, NdCrO$_3$, and LaCrO$_3$ taken from the literature [36,40].

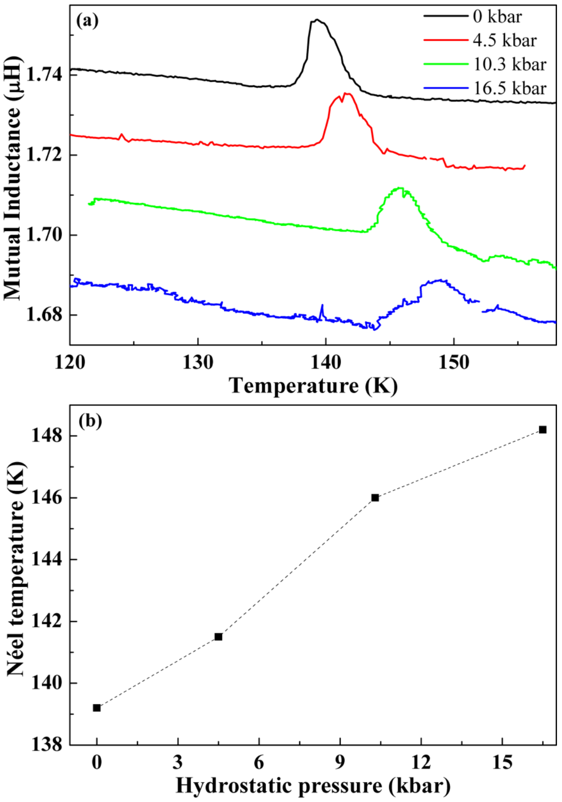

FIG. 7. (a) The temperature dependence of mutual inductance of $HoCrO_3$ pellet sample under different hydrostatic pressure (0–16.5 kbar); (b) Néel temperature (T_N^{Cr}) of $HoCrO_3$ sample as a function of the hydrostatic pressure. The line joining the points in (b) is drawn for visual clarity.

Tm^{3+}, Gd^{3+}, and Cr^{3+} (3.8 μ_B) [16], with $x = 0.33$

$$\mu_{\rm eff}{}^a = \sqrt{\mu_{\rm Cr}^2 + (1-x)\mu_{\rm Ho}^2 + x\mu_{\rm Gd,Tm}^2}. \quad (3)$$

Magnitudes of all these parameters (T_N^{Cr}, C, θ, $\mu_{\rm eff}$, and $\mu_{\rm eff}{}^a$) determined from the above analysis are summarized in Table IV. The excellent agreement between $\mu_{\rm eff}$ and $\mu_{\rm eff}{}^a$ values found for all compositions confirms the correctness of the employed procedures and the chemical composition and phase purity of the samples.

From Figs. 8(a)–8(c), it is evident that the CW fitting works well in the high temperature regime well above T_N^{Cr} but fails near or below T_N^{Cr}. This is because the present samples exhibit weak FM below T_N^{Cr} and are canted antiferromagnets instead of simple antiferromagnets. This weak FM is due to the Dzyaloshinskii-Moriya (DM) antisymmetric exchange interaction whose effect was included by Moriya on the temperature dependence of the paramagnetic susceptibility using a molecular field approximation [52]. According to this theory, the susceptibility in the easy-axis direction obeys the CW law, whereas the susceptibility perpendicular to the easy axis also depends on the DM interaction. Since the susceptibility in the direction parallel and perpendicular to the easy axis could not be measured separately for the present polycrystalline samples, we use the equations for the dominant contribution from the perpendicular direction, as modeled by Moriya [52],

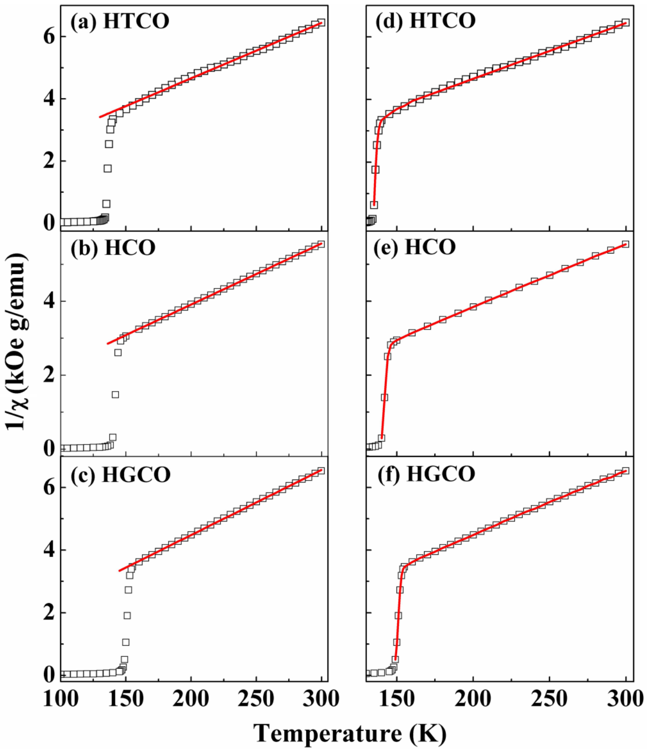

FIG. 8. Temperature dependence of inverse susceptibility ($1/\chi$) of (a) $Ho_{0.67}Tm_{0.33}CrO_3$ (HTCO), (b) $HoCrO_3$ (HCO), and (c) $Ho_{0.67}Gd_{0.33}CrO_3$ (HGCO) samples, with the black squares as data points and the red solid line fits to the Curie-Weiss law. In (d)–(f), the red lines are the corresponding fits to the modified Curie-Weiss law of Eq. (4), which includes the DM interaction.

$$\chi = \frac{C'}{(T-\theta')}\frac{T-T_0}{\left(T-T_N^{Cr'}\right)}, \quad (4)$$

where T is the temperature and T_0 and $T_N^{Cr'}$ are fitting parameter, given by [52],

$$T_0 = \frac{2J_e Z S\,(S+1)}{3k_B}, \quad (5)$$

$$T_N^{Cr'} = \frac{2J_e Z S(S+1)}{3k_B}\left[1+\left(\frac{D}{2J_e}\right)^2\right]^{\frac{1}{2}}. \quad (6)$$

Here $Z = 6$ is the coordination number of Cr^{3+} relative to other Cr^{3+} ions, and $S = 3/2$ is the spin quantum number of Cr^{3+}. Equations (5) and (6) give semiquantitative analyses of J_e and D, the magnitudes of the symmetric and antisymmetric Cr^{3+}-Cr^{3+} exchange interactions, respectively. The Cr^{3+}-Cr^{3+} exchange interactions can be extracted from the above parameters, as T_N^{Cr} is far above the rare-earth ordering temperature where other exchange interactions (R^{3+}-R^{3+} and R^{3+}-Cr^{3+}) are ignorable. In Figs. 8(d)–8(f), the plots of $1/\chi$ versus T data for the three samples approaching T_N^{Cr} for $T > T_N^{Cr}$, along with the fits to Eq. (4) are shown. Note that the magnetization data were measured in an interval of 0.5 K near T_N^{Cr} in order to provide a better test for the model. All the fitted parameters listed in Table IV, such as Curie constant (C'), T_0, Weiss

TABLE IV. The magnetic parameters: Cr^{3+} ordering temperature T_N^{Cr}(K), the Weiss temperature θ (K), Curie constant C (emu K Oe^{-1} mol^{-1}), and effective magnetic moment $\mu_{eff}(\mu_B)$ obtained by Curie-Weiss fit of the susceptibility data; the $T_N^{Cr\prime}$ (K), θ'(K), C' (emu K Oe^{-1} mol^{-1}), the fitting parameter T_0(K), the symmetric exchange constant J_e(K), and the antisymmetric exchange constant D_e resulting from the modified Curie-Weiss fitting the dc susceptibility data. $\mu_{eff}{}^a$ is calculated by free ionic moments of Cr^{3+} and Ho^{3+} ions.

Samples	$Ho_{0.67}Tm_{0.33}CrO_3$	$HoCrO_3$	$Ho_{0.67}Gd_{0.33}CrO_3$
T_N^{Cr}(K)	135.0(1)	139.2(2)	148.5(1)
C (emu K Oe^{-1} mol^{-1})	13.07(5)	17.01(4)	13.10(4)
θ (K)	– 27.68(81)	– 36.47(60)	– 15.48(77)
$\mu_{eff}(\mu_B)$	10.22(2)	11.66(1)	10.23(2)
$\mu_{eff}{}^a(\mu_B)$	10.29	11.23	10.63
$T_N^{Cr\prime}$ (K)	135.2(1)	139.9(2)	149.7(4)
T_0 (K)	134.4(2)	141.7(2)	150.4(1)
J_e/k_B (K)	8.96(1)	9.44 (1)	10.02(1)
D/k_B(K)	1.92(3)	1.23(6)	1.41(2)
θ' (K)	– 80.3(4)	– 29.1(5)	– 25.2(3)
C' (emu K Oe^{-1} mol^{-1})	15.73(2)	17.01(4)	13.10(4)
μ'_{eff} (μ_B)	10.62(8)	11.21(10)	10.20(6)

temperature (θ'), and temperature ($T_N^{Cr\prime}$) are close to those obtained using a CW fit and $d(\chi T)/dT$ versus T plot.

The above analysis shows that the exchange constant $J_e/k_B = 8.96$ K, 9.44 K, and 10.02 K determined, respectively, for the three samples of HTCO, HCO, and HGCO discussed here increases in the same order as the Cr1-O1-Cr1 bond angles listed in Table I for these samples. This is understandable since the Cr-Cr superexchange coupling depends on this bond angle as well as Cr1-O1 bond lengths. This correlation between the structural properties and magnetic properties is considered to be an important result of this paper.

An interpretation of the observed increase in T_N^{Cr} of HCO with increase in applied hydrostatic pressure shown in Fig. 7 is considered next. Using Raman spectroscopy as a probe, Bhadram *et al.* [31] have reported on the changes in the octahedral distortions under hydrostatic pressure in several $RCrO_3$ systems (R = Lu, Tb, Gd, Eu, Sm). These octahedral distortions with increase in hydrostatic pressure result in changes in the Cr1-O1-Cr1 bond angle and Cr1-O1 bond lengths, which in turn affects the exchange coupling and hence the measured T_N^{Cr}. Their main conclusion from these investigations was that pressure dependence of T_N^{Cr} in $RCrO_3$ (R = Gd, Eu, Sm) is largely due to due to the compression of the Cr1-O1 bonds rather than changes in the Cr1-O1-Cr1 bond angle. Extending this argument to the three samples investigated here, it would appear that the results of the changes in T_N^{Cr} with chemical doping and hydrostatic pressure have slightly different origins, the former dominated by changes in the Cr1-O1-Cr1 bond angle and the latter dominated by and Cr1-O1 bond lengths. The calculation of super-exchange constant from first principles is usually quite difficult since it requires exact knowledge of the wave functions involved. However, semiquantitative determination of changes in J_e under hydrostatic pressure and chemical doping might be possible using modern density functional theory (DFT) codes.

To investigate the dependence of magnetization (M) on magnetic field (H), isothermal M–H curves were measured between 5 and 145 K for the three samples; these results are shown in Figs. 9(a)–9(c). At $T = 5$ K and $H = 40$ kOe (4 Tesla), magnetization values for HTCO, HCO, and HGCO bulk samples are 69.3, 86.0, and 96.3 emu g^{-1}, respectively. Clearly, the magnitude of M decreases with Tm doping, but it increases with Gd doping. These changes in the magnitudes of M on chemical doping correlate well with the observed changes in T_N^{Cr}, which in turn depend on the changes in the Cr1-O1-Cr1 bond angle. Note that in Table I, the observed changes in the Cr1-O1-Cr1 bond angle on Gd doping are much larger than those observed with Tm doping, similar to the observed changes in the magnetic parameters for these systems (Table IV).

The measured M–H curves at lower temperatures in Fig. 9 are not linear. This low temperature nonlinearity is due to the presence of a weak ferromagnetic component resulting from the canting of the Cr^{3+} moments, whereas the linear component is due to paramagnetism of Ho^{3+} ions (above its ordering temperature) and the underlying antiferromagnetism of Cr^{3+} ions. With increase in temperature from 5 K, the weak ferromagnetic component decreases in strength as expected, and M–H curves becomes increasingly linear, as evident at the $T = 145$ K for HCO sample due to the presence of paramagnetism of Cr^{3+} ions above T_N^{Cr}.

D. Magnetocaloric properties

The isothermal M versus H data presented in Fig. 9 is used next to determine the magnetocaloric properties of the present samples that can be defined in terms of the three parameters. The first is the magnetic entropy change (ΔS, where sometimes 'M' is used as subscript to denote *magnetic* entropy change), which can be derived from the Maxwell relation [53],

$$\Delta S(T,H) = \int_0^H \left(\frac{\partial M(T,H)}{\partial T}\right)_H dH \approx \sum_i \frac{M_{i+1}(T_{i+1},H)\text{-}M_i(T_i,H)}{T_{i+1}\text{-}T_i}\Delta H. \quad (7)$$

Since the magnetization is measured in discrete field and temperature intervals, ΔS can be approximately calculated by the summation from the isothermal M versus H curve in Fig. 9. The second parameter is the refrigeration capacity (RC), which is the amount of heat transfer between the cold

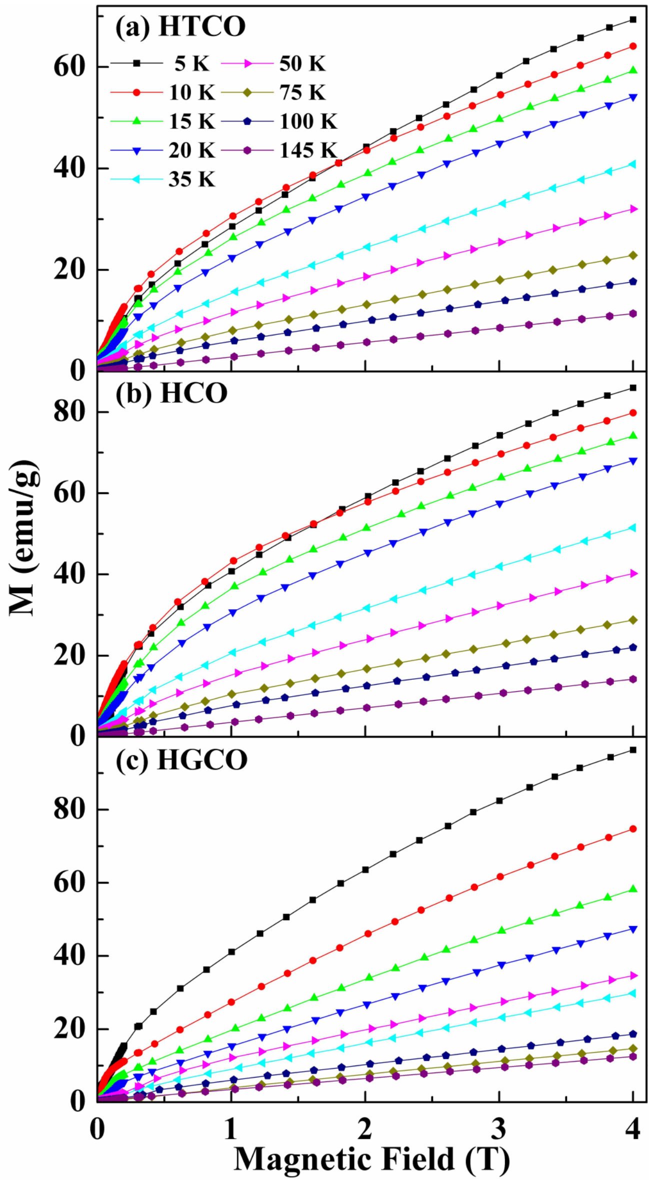

FIG. 9. Isothermal magnetization (M) data versus applied magnetic field (in first quadrant) at select temperatures between 5 K and 145 K for (a) $Ho_{0.67}Tm_{0.33}CrO_3$ (HTCO), (b) $HoCrO_3$ (HCO), and (c) $Ho_{0.67}Gd_{0.33}CrO_3$ (HGCO) samples. The lines joining the data points are visual guides.

and hot reservoirs in a magnetic refrigerator, and is defined by Eq. (8),

$$RC = \int_{T_1}^{T_2} |\Delta S_{M,H}| dT, \tag{8}$$

where T_1 and T_2 are the temperature of the cold and hot reservoirs, respectively. The refrigeration efficiency of a material is mainly dependent on RC. The third parameter is the adiabatic temperature change (ΔT_{ad}), calculated using Eq. (9) [54],

$$\Delta T_{\text{ad}} = \mu_0 \int_0^H \frac{T}{C_H} \left(\frac{\partial M}{\partial T} \right)_H dH \approx \frac{T}{C_P} \Delta S. \tag{9}$$

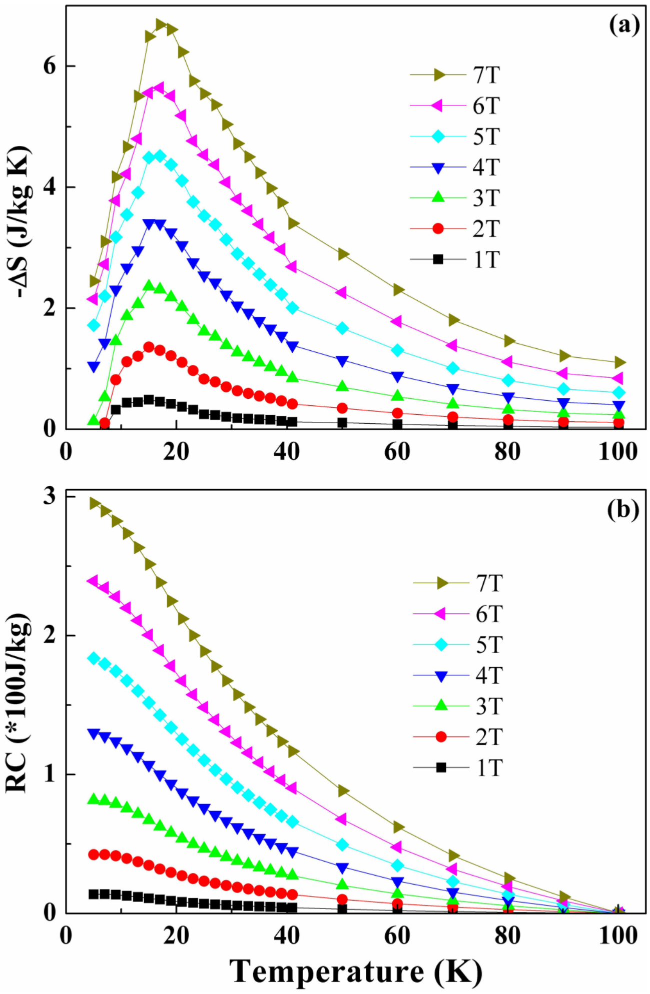

FIG. 10. The temperature dependence of (a) entropy change (ΔS) and (b) refrigeration capacity (RC) of $Ho_{0.67}Tm_{0.33}CrO_3$ (HTCO) sample in magnetic fields up to 7T (70 kOe).

The above approximation was based on the precondition that T/C_H shows little dependence on the magnetic field, as reported by Su *et al.* [55]. The maximum ΔT_{ad} is calculated using $C_H/T \approx 0.8\,\text{J/(mol K}^2)$ at ~20 K for HCO.

In Fig. 10(a), the representative thermal variation of ΔS of the HTCO sample at various applied fields ($H = 1$ to 7 T) is presented. It is evident that at a given temperature, magnitudes of ΔS increase with an increase in magnetic field since a larger magnetic field induces a larger magnetization thus leading to larger ΔS (see Eq. (7)). With an increase in temperature from 5 K, the magnitude of ΔS of HTCO first increases, reaching a maximum at ~17 K, and decreases thereafter. The maximum magnitude of ΔS of HTCO obtained is 6.7 J/kg K at 17 K and at $H = 7$ T. For comparison, $\Delta S \sim 4.6$ J/kg K at $H = 5$ T and $T = 10$–20 K for the pure $TmCrO_3$ powder sample was reported [35], which is similar to $\Delta S \sim 4.5$ J/kg K under 5 T and 17 K for HTCO sample.

Figure 10(b) shows the RC value of the present HTCO sample (where $T_1 = 5$ K and $T_2 = 100$ K). Like ΔS, the RC value also increases with increasing magnetic field from 1 T to 7 T. At 7 T, the RC value of the present HTCO sample is

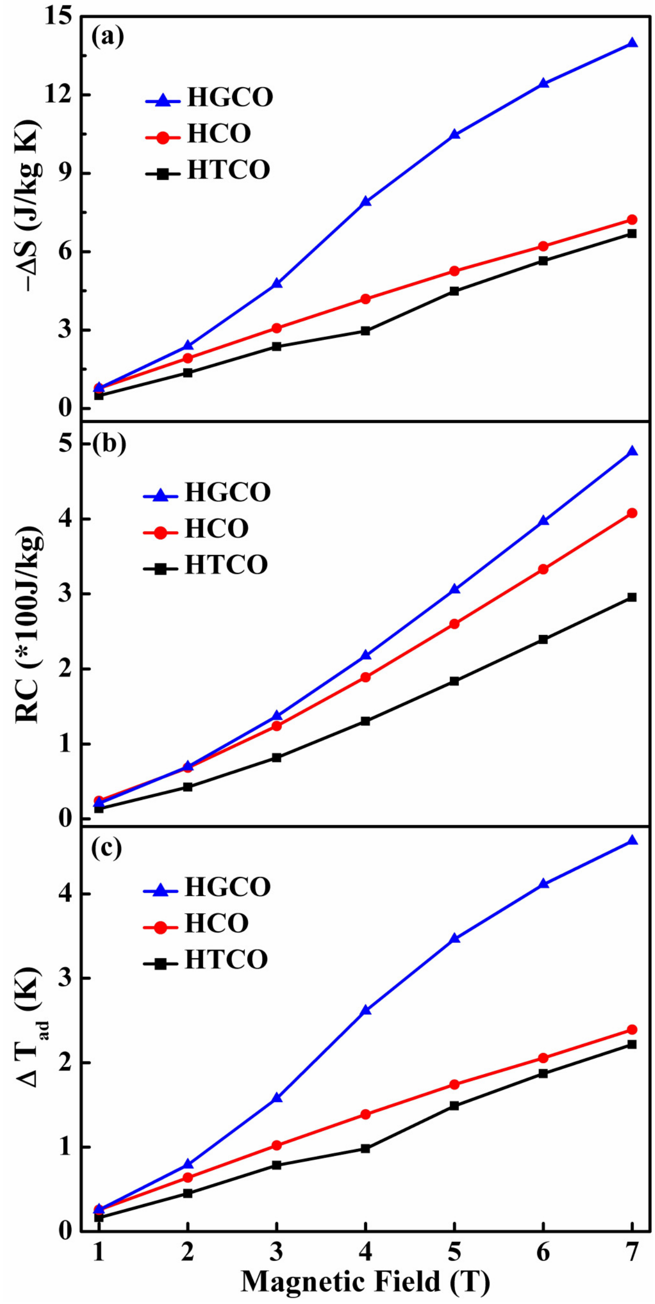

FIG. 11. (a) The maximum of magnetic entropy change ($-\Delta S$), (b) refrigeration capacity (RC), and (c) adiabatic temperature change (ΔT_{ad}) as a function of magnetic field for $\mathrm{Ho_{0.67}Tm_{0.33}CrO_3}$ (HTCO), $\mathrm{HoCrO_3}$ (HCO), and $\mathrm{Ho_{0.67}Gd_{0.33}CrO_3}$ (HGCO) samples. The lines joining the data points are visual guides.

295.3 J/kg, compared to 86 J/kg for $\mathrm{TmCrO_3}$ sample under $H = 5\,\mathrm{T}$ ($T_1 = 5\,\mathrm{K}$ and $T_2 = 25\,\mathrm{K}$) [35].

To compare the magnetocaloric characteristics of the three samples investigated here, the magnetic field dependence of ΔS, RC, and ΔT_{ad} for the three samples is presented in Fig. 11. Note that the magnitudes of these quantities for each sample increase with increasing applied magnetic field. As such, the nature of their field dependence is very similar, although the specific values differ. Notably, magnitudes of ΔS, RC, and ΔT_{ad} of the HCO sample are larger than those of HTCO but smaller than those of HGCO. Hence, Tm doping was found to lower the magnetocaloric properties of HCO, whereas Gd doping was found to enhance these properties. This trend follows the changes in the isothermal magnetization observed in Fig. 9 on doping HCO with Tm and Gd, suggesting that the magnitude of the magnetization may be the controlling factor. For comparison, the magnetization of $\mathrm{GdCrO_3}$ and HGCO at 5 K and 4 T are 105 emu/g [56] and 87 emu/g (Fig. 9), respectively. Similarly, for the three samples of HTCO, HCO, and HGCO, the MCE properties shown in Fig. 11 qualitatively scale with the M versus H variations observed in Fig. 9. The large MCE observed in $\mathrm{GdCrO_3}$ has been suggested to result from the large $\mathrm{Gd^{3+}}$–$\mathrm{Gd^{3+}}$ magnetic interaction, although no quantitative analysis in this regard was presented [56].

The dopant effect on MCE is likely not related to R_{avg}, since McDannald and Jain doped $\mathrm{DyCrO_3}$ powder samples on the A-site with Y, Er, and Ho, all of which have smaller R_{avg} than Dy. In that case, Y and Ho doping lowered MCE, whereas Er doping improved MCE [25]. Most likely, the enhancement in MCE by Gd doping in $\mathrm{HoCrO_3}$ in the present paper is related to the reported giant MCE of $\mathrm{GdCrO_3}$ for which the magnitude of ΔS is 27 J/kg K at 5 K and 4.4 T [56], compared to the magnitude of ΔS of about 10 J/kg K for HGCO under the same (H, T) conditions. In any case, the observed improvement of the MCE in $\mathrm{HoCrO_3}$ by Gd doping at the A-site is very encouraging and holds promise for further tuning of the MCE by optimizing the A-site dopant (both nature and content) in $R\mathrm{CrO_3}$ compounds for their potential applications in magnetic refrigeration in low-temperature region.

IV. CONCLUSIONS

In this paper, we report on the changes in structural, optical, magnetic, and magnetocaloric properties of $\mathrm{HoCrO_3}$ powder sample arising from doping at the A-site (chemical pressure) with two different ions having ionic radii smaller ($\mathrm{Tm^{3+}}$) and larger ($\mathrm{Gd^{3+}}$) than $\mathrm{Ho^{3+}}$. Three compositions studied in this paper—$\mathrm{Ho_{0.67}Tm_{0.33}CrO_3}$ (HTCO), $\mathrm{HoCrO_3}$ (HCO), and $\mathrm{Ho_{0.67}Gd_{0.33}CrO_3}$ (HGCO)—prepared by citrate route were found to crystallize in the orthorhombically distorted perovskites structure (space group of *Pbnm*). Analyses of the optical absorption spectra show direct band gaps E_g = 3.06 eV, 3.14 eV, and 2.75 eV for HTCO, HCO, and HGCO, respectively. The ordering temperature of $\mathrm{Cr^{3+}}$, $T_{\mathrm{N}}^{\mathrm{Cr}}$, was determined from the temperature dependence of magnetic susceptibility data and was found to be 139 K for HCO, which is decreased to 135 K for HTCO but increased to 148 K for the HGCO sample. These changes are related to R_{avg}, the tolerance factor, the Cr1-O1-Cr1 bond angle, and the orthorhombic strain factor, although it is argued that the Cr1-O1-Cr1 bond angle that affects the $\mathrm{Cr^{3+}}$-$\mathrm{Cr^{3+}}$ superexchange interaction is likely the controlling factor. The observed increase in $T_{\mathrm{N}}^{\mathrm{Cr}}$ of HCO with the applied hydrostatic pressure up to 16.5 kbar is qualitatively similar to doping with larger $\mathrm{Gd^{3+}}$ ion (chemical pressure) for $\mathrm{Ho^{3+}}$ ion at the A-site. However, it is argued that the results of the changes in $T_{\mathrm{N}}^{\mathrm{Cr}}$ with chemical doping and hydrostatic pressure have slightly different origins, in which the former is dominated by changes in the Cr1-O1-Cr1 bond angle and the latter is dominated by changes in Cr1-O1 bond lengths. Fitting of the temperature dependence of the paramagnetic susceptibility to the modified Curie-Weiss law, including the Dzyloshinskii-Moriya (DM) interaction, is used to determine the effect of Tm or Gd doping on T_N^{Cr}, the exchange constant J_e, and the DM interaction. The magnetic field dependent magnetization data (up to 7 T field) are used to determine the magnetocaloric properties of these samples. At $H = 7$ T, the maximum magnetocaloric entropy changes for HTCO, HCO, and HGCO are 6.69 J/kg K, 7.22 J/kg K, and 14.0 J/kg K, and their refrigeration capacities are 295 J/kg, 408 J/kg, and 490 J/kg, respectively. The large magnetocaloric entropy change observed in HoCrO$_3$ and its tunability by Tm and Gd doping makes HoCrO$_3$ a promising system for next-generation low-temperature magnetic refrigeration. Based on this encouraging result, further enhancement in MCE properties may be possible by optimizing the A-site dopant or by increasing the Gd/Ho ratio.

ACKNOWLEDGMENTS

This paper was supported in part by a research grant from the U.S. National Science Foundation (Grant No. DMR-1310149). For the optical measurements, SLS acknowledges support of the U.S. Department of Energy, Office of Basic Energy Sciences, Division of Chemical, Biological and Geological Sciences under Grant No. DE-FG02-86ER13622.A000. Pressure dependent work at Houston was supported by the US Air Force Office of Scientific Research Grant No. FA9550-09-1-0656, the T.L.L. Temple Foundation, the J.J. and R. Moores Endowment, and the State of Texas through the Texas Center for Superconductivity.

---

[1] S.-W. Cheong and M. Mostovoy, Nat. Mater. **6**, 13 (2007).
[2] G. Lawes and G. Srinivasan, J. Phys. D. Appl. Phys. **44**, 243001 (2011).
[3] J. F. Scott, NPG Asia Mater. **5**, e72 (2013).
[4] M. Mostovoy, Nat. Mater. **9**, 188 (2010).
[5] J. R. Sahu, C. R. Serrao, N. Ray, U. V. Waghmare, and C. N. R. Rao, J. Mater. Chem. **17**, 42 (2007).
[6] Z. X. Cheng, X. L. Wang, S. X. Dou, H. Kimura, and K. Ozawa, J. Appl. Phys. **107**, 09D905 (2010).
[7] M. K. Sharma, T. Basu, K. Mukherjee, and E. V Sampathkumaran, J. Phys. Condens. Matter **28**, 426003 (2016).
[8] S. Yin, T. Sauyet, M. S. Seehra, and M. Jain, J. Appl. Phys. **121**, 063902 (2017).
[9] B. Rajeswaran, D. I. Khomskii, A. K. Zvezdin, C. N. R. Rao, and A. Sundaresan, Phys. Rev. B **86**, 214409 (2012).
[10] B. Rajeswaran, P. Mandal, R. Saha, E. Suard, A. Sundaresan, and C. N. R. Rao, Chem. Mater. **24**, 3591 (2012).
[11] A. Ghosh, A. Pal, K. Dey, S. Majumdar, and S. Giri, J. Mater. Chem. C **3**, 4162 (2015).
[12] A. Ghosh, K. Dey, M. Chakraborty, S. Majumdar, and S. Giri, Europhys. Lett. **107**, 47012 (2014).
[13] P. Gupta and P. Poddar, RSC Adv. **5**, 10094 (2015).
[14] A. Jaiswal, R. Das, K. Vivekanand, T. Maity, P. M. Abraham, S. Adyanthaya, and P. Poddar, J. Appl. Phys. **107**, 013912 (2010).
[15] G. Kotnana and S. N. Jammalamadaka, J. Appl. Phys. **118**, 124101 (2015).
[16] S. Yin, V. Sharma, A. McDannald, F. A. Reboredo, and M. Jain, RSC Adv. **6**, 9475 (2016).
[17] J. Beckers and G. Rothenberg, ChemPhysChem **6**, 223 (2005).
[18] A. L. Linsebigler, G. Lu, and J. T. Yates, Chem. Rev. **95**, 735 (1995).
[19] Z. Shao, W. Zhou, and Z. Zhu, Prog. Mater. Sci. **57**, 804 (2012).
[20] S. C. Singhal, Solid State Ionics **135**, 305 (2000).
[21] N. Russo, D. Mescia, D. Fino, G. Saracco, and V. Specchia, Ind. Eng. Chem. Res. **46**, 4226 (2007).
[22] M. Siemons and U. Simon, Sensors and Actuators B. **126**, 181 (2007).
[23] A. McDannald, L. Kuna, and M. Jain, J. Appl. Phys. **114**, 113904 (2013).
[24] L. H. Yin, J. Yang, R. R. Zhang, J. M. Dai, W. H. Song, and Y. P. Sun, Appl. Phys. Lett. **104**, 032904 (2014).
[25] A. McDannald and M. Jain, J. Appl. Phys. **118**, 043904 (2015).
[26] S. Yin and M. Jain, J. Appl. Phys. **120**, 043906 (2016).
[27] N. D. Todorov, M. V. Abrashev, V. G. Ivanov, G. G. Tsutsumanova, V. Marinova, Y. Q. Wang, and M. N. Iliev, Phys. Rev. B **83**, 224303 (2011).
[28] V. Sharma, A. McDannald, M. Staruch, R. Ramprasad, and M. Jain, Appl. Phys. Lett. **107**, 012901 (2015).
[29] K. Yamauchi, F. Freimuth, S. Blügel, and S. Picozzi, Phys. Rev. B **78**, 014403 (2008).
[30] J. M. Chen, J. M. Lee, T. L. Chou, S. A. Chen, S. W. Huang, H. T. Jeng, K. T. Lu, T. H. Chen, Y. C. Liang, S. W. Chen, W. T. Chuang, H.-S. Sheu, N. Hiraoka, H. Ishii, K. D. Tsuei, E. Huang, C. M. Lin, and T. J. Yang, J. Chem. Phys. **133**, 154510 (2010).
[31] V. S. Bhadram, D. Swain, R. Dhanya, M. Polentarutti, A. Sundaresan, and C. Narayana, Mater. Res. Express **1**, 026111 (2014).
[32] H. J. Zhao, W. Ren, Y. Yang, X. M. Chen, and L. Bellaiche, J. Phys. Condens. Matter **25**, 466002 (2013).
[33] H. J. Zhao, W. Ren, X. M. Chen, and L. Bellaiche, J. Phys. Condens. Matter **25**, 385604 (2013).
[34] C. W. Chu and L. R. Testardi, Phys. Rev. Lett. **32**, 766 (1974).
[35] K. Yoshii, Mater. Res. Bull. **47**, 3243 (2012).
[36] J. Prado-Gonjal, R. Schmidt, J. J. Romero, D. Ávila, U. Amador, and E. Morán, Inorg. Chem. **52**, 313 (2013).
[37] A. L. Patterson, Phys. Rev. **56**, 978 (1939).
[38] P. Dutta, M. S. Seehra, S. Thota, and J. Kumar, J. Phys. Condens. Matter **20**, 015218 (2008).
[39] M. Wojdyr, J. Appl. Cryst. **43**, 1126 (2010).
[40] M. C. Weber, J. Kreisel, P. A. Thomas, M. Newton, K. Sardar, and R. I. Walton, Phys. Rev. B **85**, 054303 (2012).
[41] V. S. Bhadram, B. Rajeswaran, A. Sundaresan, and C. Narayana, Europhys. Lett. **101**, 17008 (2013).
[42] J. Tauc, Mater. Res. Bull. **3**, 37 (1968).
[43] W. W. Kou and M. S. Seehra, Phys. Rev. B **18**, 7062 (1978).
[44] K. M. Parida, A. Nashim, and S. K. Mahanta, Dalton Trans. **40**, 12839 (2011).

[45] T. Arima, Y. Tokura, and J. B. Torrance, Phys. Rev. B **48**, 17006 (1993).

[46] K. P. Ong, P. Blaha, and P. Wu, Phys. Rev. B **77**, 073102 (2008).

[47] S. Saha, S. Chanda, A. Dutta, and T. P. Sinha, J. Sol-Gel Sci. Technol. **69**, 553 (2014).

[48] A. McDannald, L. Kuna, M. S. Seehra, and M. Jain, Phys. Rev. B **91**, 224415 (2015).

[49] N. Poudel, M. Gooch, B. Lorenz, C. W. Chu, J. W. Kim, and S. W. Cheong, Phys. Rev. B **92**, 144430 (2015).

[50] J. A. Alonso, M. J. Martínez-Lope, and M. T. Casais, Inorg. Chem. 2000, **39**, 917 (2000).

[51] J. M. D. Coey, *Magnetism and Magnetic Materials* (Cambridge University Press, Cambridge, 2009).

[52] T. Moriya, Phys. Rev. **120**, 91 (1960).

[53] M. H. Phan and S. C. Yu, J. Magn. Magn. Mater. **308**, 325 (2007).

[54] V. K. Pecharsky and K. A. Gschneidner, J. Appl. Phys. **86**, 565 (1999).

[55] Y. Su, J. Zhang, Z. Feng, Z. Li, Y. Shen, and S. Cao, J. Rare Earths **29**, 1060 (2011).

[56] L. H. Yin, J. Yang, X. C. Kan, W. H. Song, J. M. Dai, and Y. P. Sun, J. Appl. Phys. **117**, 133901 (2015).